CHEMISTRY OF MATERIALS

ARTICLE

pubs.acs.org/cm

Synthesis and Study of a Ce-Doped La/Sr Titanate for Solid Oxide Fuel Cell Anode Operating Directly on Methane

Cédric Périllat-Merceroz,[†,‡,§] Gilles Gauthier,[⊥,†,*] Pascal Roussel,[‡] Marielle Huvé,[‡] Patrick Gélin,[§] and Rose-Noëlle Vannier[‡]

[†]CEA/LITEN, Laboratoire d'Innovation Technologique et des Energies Nouvelles, 17 rue des Martyrs, F-38054 Grenoble, France

[‡]Université Lille Nord de France, CNRS, UMR8181, UCCS, Unité de Catalyse et de Chimie du Solide, ENSCL-Université Lille 1, BP90108, F-59652 Villeneuve d'Ascq, France

[§]Université Lyon 1, CNRS, UMR5256, IRCELYON, Institut de recherches sur la catalyse et l'environnement de Lyon, 2 avenue Albert Einstein, F-69626 Villeurbanne, France

ABSTRACT: The possibility to introduce cerium in the perovskite-type titanate with formula $La_{0.33}Sr_{0.67}TiO_{3+\delta}$ (LST) was investigated. Pure-phased $La_{0.23}Ce_{0.1}Sr_{0.67}TiO_{3+\delta}$ (LCST) was only obtained by synthesis at high temperature in reducing (diluted hydrogen) atmosphere. The material exhibits the same orthorhombic symmetry with *Immm* space group as LST and nearly the same cell volume. When exposed to oxidizing atmosphere at 1200 °C, Ti^{3+} and Ce^{3+} oxidation leads to the decomposition of LCST and the growth of several nanoscaled Ce-rich phases, as highlighted by backscattered electron microscopy. Shifting the gas back to a reducing atmosphere, but at lower temperature, only involves partial reversibility, ensuring the presence of nanoparticles of (electro)catalytically active phase within an electronically conducting n-type network. The catalytic tests in methane steam reforming at 900 °C (CH_4/H_2O = 10/1) show that the properties of the partially decomposed phase are greatly improved, what could make it a promising anode material for SOFC operating on slightly wet methane.

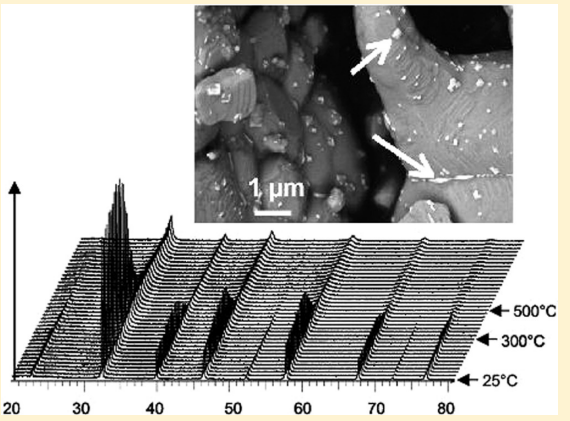

KEYWORDS: SOFC anode, perovskite, titanate, ceria, exsolution, catalysis, steam reforming

INTRODUCTION

One of the most serious issues the world will have to face in the next century is without any doubt the emission of greenhouse effect gases that leads to the so-called Anthropogenic Global Warming of the Earth lower atmosphere. To limit the human activity influence, energy production alternatives such as Solid Oxide Fuel Cells (SOFC) are required. Because of its high thermodynamic efficiency, that is, comparatively low environmental impact, this kind of electrochemical system seems to be one of the most promising solutions, by using hydrogen containing fuels to replace hydrocarbon combustion.

One particular issue that has still to be addressed in SOFCs is to reduce the degradation of Ni-based materials when realistic fuels like Natural Gas are directly used at the anode side. Waiting for large scale production of hydrogen from renewable sources, the use of such already available fuel would give the opportunity to extend at short and middle term the SOFC commercialization. Nowadays, the major problems with Ni-YSZ cermets are indeed the irreversible losses of activity stemming from (i) carbon deposition, (ii) poisoning by sulfur containing compounds, (iii) growth of Ni-particles, and (iv) redox cycling, the latter two points being true even in H_2/H_2O atmospheres.[1−3]

Use of hydrocarbon-containing fuel in SOFCs, and in particular natural gas, is called in this case direct utilization or direct oxidation. In reality, there has been some controversy about whether direct, electrochemical oxidation proceeds or some steps of the overall mechanism involve purely catalytic reactions, such as steam reforming to form H_2 as an intermediate product, because of the coexistence of hydrocarbon and steam at the anode.[4] Steam can be either added or produced, acting in the latter case as a reactant for steam reforming; this advantage has led to the development of Gradual Internal Reforming concept, which is a natural consequence of cell operation with C (and H)-containing fuels.[5] As pointed out by some groups,[4,6] direct electro-oxidation of hydrocarbons seems unlikely without a contribution from catalysis according to which the hydrocarbon could be activated through the C−H and C−C bond scission. Being determining in the mechanism or not, the catalytic contribution cannot be ruled out and a relationship, although possibly complex, must exist between electrocatalysis and catalysis. In this respect, when considering the further development of fuel cells operating directly on natural gas, it appears necessary

Received: November 18, 2010
Revised: February 2, 2011
Published: February 28, 2011

to us to evaluate the catalytic properties of new anode components in steam reforming with low steam content ($CH_4/H_2O \gg 1$) and not in pure methane, which is never the case in stationary conditions. Indeed, this reaction is particularly relevant to estimate the ability of the material to activate the highly stable methane molecule. Furthermore, the use of strongly water deficient conditions for this test reaction would allow discriminating between materials depending on their activity but also their tendency to develop extensive carbon formation, which is known to be detrimental to the proper operation of the fuel cell. The latter point has been an issue for recent developments in anode materials of fuel cell operating on direct use of hydrocarbon.

Among possible alternating materials, titanate perovskites and especially donor-doped $SrTiO_3$ have been considered in replacement of Ni-based cermets at the anode side of SOFCs because of their high resistance toward reducing and sulphured atmospheres, as well as redox stability. To increase the too low conductivity displayed by $Sr^{+II}Ti^{+IV}O_3$, the partial substitution of Sr^{2+} by a trivalent ion, such as La^{3+} or Y^{3+}, is judged as the best way up to now.[7−13] Indeed, under reducing conditions, the presence of trivalent ions in A-sites of the perovskite makes the Ti^{4+} ($3d^0$) → Ti^{3+} ($3d^1$) reduction easier, thus enhancing the electronic charge carrier concentration. Very promising performances in terms of n-type conductivity were notably obtained under reducing atmosphere in the case of $La_{0.33}Sr_{0.67}TiO_{3+\delta}$, the $x = 0.33$ compound of the $La_xSr_{1-x}TiO_{3+\delta}$ family.[14,15]

In terms of catalytic (hydrocarbon reforming or oxidation), as well as electrocatalytic (hydrogen electrochemical oxidation) behavior, La- or Y-doped-Sr titanates display a very poor activity and generally require the addition of a catalyst and/or electrocatalyst.[9,16−19] To enhance these properties, ceria-based compounds are of interest since these materials are known to play an important role in fuel cells directly operated on methane but also in catalysis for water gas shift and steam reforming reactions.[4,6,20−26] Effectively, attempts to associate LST to Ce-containing materials have been carried out, leading to improved performance of the anode without carbon deposition even in severe coking conditions; but in those cases, composite materials with doped ceria and doped strontium titanate apart were only considered.[18,27−29]

The aim of the present paper is to investigate the possibility of improving the catalytic and electrocatalytic properties of LST materials by introducing the Ce^{4+}/Ce^{3+} redox couple through partial substitution of La by Ce in the structure of the $x = 33$ member of the $La_xSr_{1-x}TiO_{3+\delta}$ series. The structural stability of the host and substituted perovskite structures was studied by high-temperature XRD (HT-XRD) in oxidizing and reducing atmospheres at various temperatures up to 1000 °C. Catalytic properties in CH_4/H_2O reaction for H_2 production using extremely severe coking conditions (steam-to-carbon ratio equal to 10) were measured to address both the influence of Ce substitution on the catalytic activity and the resistance to carbon formation in view of the possible use of this material as a SOFC anode operating directly on methane.

EXPERIMENTAL SECTION

Compounds of stoichiometry $La_{0.33}Sr_{0.67}TiO_{3+\delta}$ (hereafter LST) and $La_{0.23}Ce_{0.1}Sr_{0.67}TiO_{3+\delta}$ (hereafter LCST) were synthesized using the standard Pechini route.[30] Ti^{4+} aqueous solution was prepared from titanium (+IV) isopropoxide (Alfa Aesar, 99.995%) mixed with ethylene glycol and citric acid in the 1:20:5 molar ratio. About 0.5 mL of deionized water per gram of citric acid was added to help citric acid dissolution. La_2O_3 (Rhodia, 99.99%), $SrCO_3$ (Alfa Aesar, 99.9%), and Ce nitrate solution (made from $Ce_2(CO_3)_3$, Alfa Aesar (99.9%)) were used in stoichiometric quantities. Nitric acid was regularly poured until the dissolution of the precursors was achieved, without any pH adjustment.

Evaporation of the solutions was carried out on a magnetic stirring plate until obtaining perfect gels. These gels were then dried and pyrolyzed in an oven overnight at 250 °C. After grinding, the resulting powders were calcined in air at 700 °C for 5 h in order to remove the excess of nitrated and carbonated residues. After grinding, the powders were pressed into pellets before being sintered at 1400 °C for 48 h in air or $Ar/H_2(2\%)$. During sintering, the pellets were put on sacrificial beds of powder made of the same composition and lying on Pt or Al_2O_3 foils.

Powder X-ray diffraction (XRD) data were collected at room temperature (RT) using a Bruker AXS D8 Advance diffractometer working in Bragg−Brentano geometry and equipped with a secondary graphite monochromator and a scintillation detector. Cu $K\alpha_{1,2}$ radiations were used in the range $2\theta = 15-120°$, with a 0.02° step and a 10 s counting time per step, respectively. The Fullprof Suite program was used for Rietveld refinement, using the Thompson-Cox-Hastings Pseudo-Voigt profile function.[31] The atomic positions as well as the isotropic atomic displacements of all atoms were refined. The small oxygen excess corresponding to $(La,Ce)_{0.33}Sr_{0.67}TiO_{3+\delta}$ formula is not taken into account in the refinement and full occupation of all the cationic and anionic sites is considered (see above in Discussion part for explanation about the defect chemistry in those phases).

High-temperature XRD (HT-XRD) was performed on a Bruker AXS D8 Advance diffractometer equipped with a high temperature Anton Paar HTK 1200N chamber and a one-dimensional X-ray detector (VÅNTEC-1) using Cu $K\alpha_{1,2}$ radiation. Samples were placed on a platinum sheet to avoid any reaction with the alumina sample holder. Data were collected in the range $2\theta = 20-80°$, with a 0.015° step and a 0.2 s counting time per step, from RT to 1000 °C in air and from RT to 800 °C in $N_2/H_2(3\%)$. Diffraction patterns were recorded every 25 °C on heating up and cooling down with the same heating and cooling rate of 0.1 °C s^{-1}. Selected area electron diffraction (SAED) patterns were obtained on a Philips CM30 transmission electron microscope. Materials were crushed and dispersed on a holey carbon film deposited on a Cu grid. X-ray Photoelectron Spectroscopy (XPS) analysis was performed on a VG ESCALAB 220XL spectrometer. Thermogravimetric analyses (TGA) were carried out in air using a SETARAM TG 92-16.18 device equipped with a 1300 μL-Pt crucible (about 1 g of sample). Heating and cooling rates were 2 and 4 °C min^{-1}, respectively, with an isotherm plateau for 2 h at 1450 °C. Scanning electron microscope (SEM) images were taken with a ZEISS Leo 1530 GEMINI using a Schottky field emission gun (FEG) and a Centaurus detector. Backscattered electrons mode (BSE) was used in order to reveal chemical contrasts. Energy dispersive spectroscopy (EDS) was carried out with a Si−Li detector fitted with a standard Be window (Princeton Gamma-Tech Instruments). The acquisition time of each spectrum was kept relatively low to avoid any signal drift.

For catalytic tests, the powders were ground in a tungsten carbide vibrating mill and sifted between 40 and 50 μm in order to control gas diffusion. Their specific surface area was determined by BET nitrogen adsorption using a Beckman Coulter SA3100 analyzer. Catalytic activity experiments were carried out in a continuous flow system at atmospheric pressure using a tubular U-shaped quartz microreactor. Blank experiments (without any sample) were performed to check that the reactor was nonreactive. Samples (about 20 mg) were deposited onto a quartz plug introduced into the reactor and renewed for each test. A thermocouple was placed in contact with the external wall of the reactor at the position in front of the catalyst bed, allowing the control of the catalyst temperature. The oxidized and the $Ar/H_2(2\%)$ reduced samples were

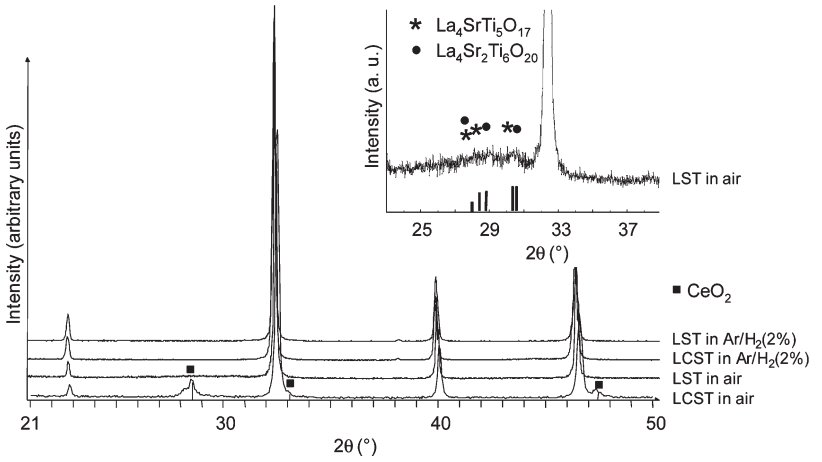

Figure 1. XRD diagrams of LST and LCST after synthesis in air, and synthesis in Ar/H_2(2%). Squares indicate CeO_2 peaks. The zoom is focused on the region where traces of $La_4SrTi_5O_{17}$ and $La_4Sr_2Ti_6O_{20}$ (the n = 5 and n = 6 members of the lamellar family $La_4Sr_{n-4}Ti_nO_{3n+2}$, respectively[14]) are observed in LST synthesized in air.

pretreated in N_2 and H_2 (6.5 L h^{-1}) at 900 °C for 2 h before catalytic test. The reactant mixture consisted of 50 mol % CH_4 and 5 mol % H_2O, N_2 as balance (total flow rate = 6.2 L h^{-1}). Suitable H_2O concentrations were obtained by flowing the adequate mixture of CH_4 and N_2 dry gases throughout a saturator containing distilled water maintained at 33 °C (thermostatted bath). Water content was determined using an Edgetech Dew Prime I dew point monitor placed nearby the reactor outlet. An ECP-type (M&C) gas cooler was used to trap most of the water vapor thus allowing gas analysis by a Varian micro-GC equipped with appropriate columns (molecular sieve 5A and Porapak) and a thermal conductivity detector. For all tests, differential conditions were fulfilled and rates of products formation could be derived. The nature and concentration of the carbonaceous species which could have formed during the catalytic measurements were studied by temperature-programmed oxidation experiments in O_2 (hereafter O_2-TPO) using a Pfeiffer Omnistar quadrupole spectrometer. The procedure was as follows. After each test, the reactor was purged in N_2 at 900 °C, cooled down to room temperature, isolated using 2 valves before being removed from the experimental setup. This allowed preventing sample exposure to air after testing. The reactor was then installed on the O_2-TPO experimental set up and purged in He at room temperature. The sample was then exposed to a 1% O_2/He flow (1.8 L h^{-1}) at room temperature until completion of eventual O_2 consumption. Afterward, the sample was heated from room temperature up to 900 °C at the rate of 20 °C min^{-1}. 1% CO/He and 1% CO_2/He mixtures were used for calibration.

RESULTS

Structural Characterization of LST and LCST at Room Temperature. After sintering at 1400 °C in air, pure phases were never obtained for both compositions. The Ce-free compound diffraction pattern of LST displayed a two-phase mixture that corresponds to a single perovskite phase coexisting with traces of lamellar compounds (Figure 1). In contrast, the powder X-ray diffractogram of the Ce-containing compound, LCST, showed evidence of impuritiy which could be indexed as cubic CeO_2. However, sintering the powder at the same temperature in a reducing atmosphere allowed the achievement of a single phase material for both compounds (Figure 1).

In agreement with Canales-Vásquez et al. for LST compounds,[14] SAED of the LCST powder, obtained under reducing conditions, evidenced the presence of additional spots

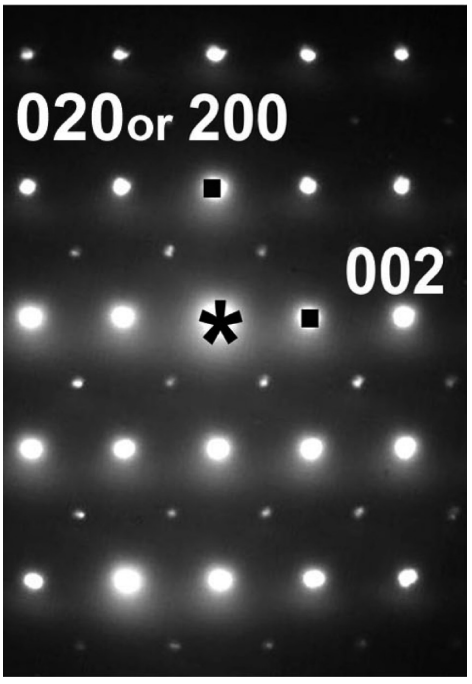

Figure 2. [010] or [100] zone axis pattern of LCST synthesized in Ar/H_2(2%), indexed in the orthorhombic $(2)^{1/2}a_p x (2)^{1/2}a_p x 2a_p$ unit cell. The deduced extinction symbol is I---.

when compared to the ideal cubic perovskite, described in the $Pm\bar{3}m$ space group ($a_p \approx 3.9$ Å). These reflections are consistent with a doubling of the c parameter ($c \approx 2a_p$) and an I Bravais lattice (Figure 2).

In a first step, a whole pattern matching of the XRD diagram was successfully obtained with the *Ibmm* space group, which is a subgroup of the ideal $Pm\bar{3}m$ perovskite via a first-order phase transition and relates to the loss of two 4-fold axes.[32,33] These results are coherent with the literature data, where only X-ray powder diffraction was used: indeed, the $La_{1-x}Sr_xTiO_3$ and $Ce_{1-x}Sr_xTiO_3$ families, extensively studied by J.E. Sunstrom IV et al., display this orthorhombic symmetry with *Ibmm* space group for $0.3 < x < 0.8$ and $0.4 < x < 0.8$, respectively.[34,35]

dx.doi.org/10.1021/cm103316b |*Chem. Mater.* 2011, 23, 1539–1550

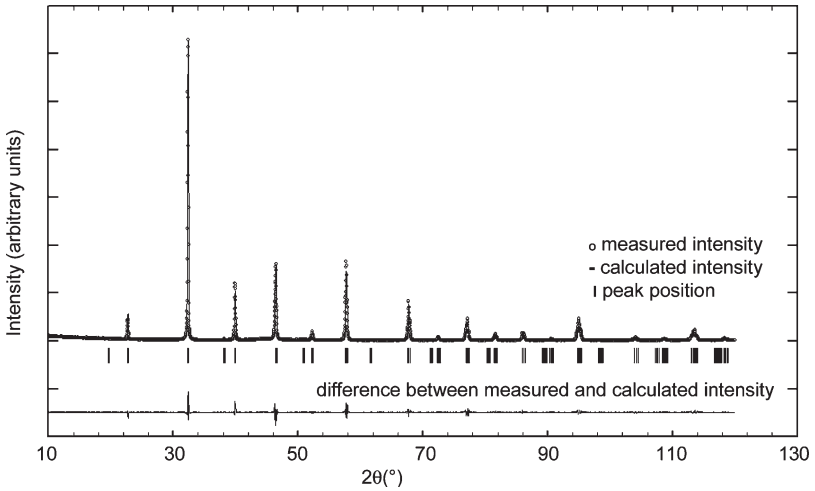

Figure 3. Rietveld refinement performed in the orthorhombic *Immm* symmetry on the XRD powder data of LCST after synthesis at 1400 °C/48 h in $Ar/H_2(2\%)$.

However, a careful examination of the SAED pattern clearly indicates the presence of $0kl$ $k = 2n + 1$ spots and consequently leads us to exclude the possibility of the *b* glide plane, and to choose a space group compatible with the I--- extinction symbol. A Rietveld refinement of the structural data was then undertaken with the highest symmetry space group compatible with the extinction rules observed by SAED, that is, *Immm*, for the two compounds prepared under reducing atmosphere. The good agreement between experimental and calculated patterns is illustrated in Figure 3 for LCST, and full crystallographic results are reported in Table 1 for LST and LCST. Refinements led to close unit-cell parameters for both compositions.

These two materials were then characterized by XPS. A focus on Ce_{3d} and Ti_{2p} measured on LCST is given in Figure 4. It excludes the presence of any amount of Ce^{4+} at the sample surface: the peaks at 885 and 908 eV are characteristic of Ce^{3+}.[36,37] The Ti_{2p} region shows a strong peak at ~458 eV, which is an overlap of Ti^{3+} and Ti^{4+} contributions. Despite the strong convolution between the two contributions, the fit of the spectrum led to an approximated Ti^{4+}/Ti^{3+} ratio of 3/1 for both compounds.[38]

Structural Study of LST and LCST versus Temperature in Reducing Atmosphere. The characterization in temperature of both LST and LCST compositions by SAED (secondary vacuum) revealed a change in symmetry from orthorhombic *Immm* to cubic $Pm\bar{3}m$ at 500 °C (Figure 5). The transformation was confirmed by HT-XRD under $N_2/H_2(3\%)$ atmosphere (Figure 6).

Unit-cell parameters were refined by cyclic profile refinements of the HT-XRD patterns. Their evolution versus temperature is given in Figure 7, with error bars showing three standard deviations (mean parameter $\pm 3\sigma$).

The change in symmetry is not direct but occurs via a tetragonal form, possibly of $I4/mcm$ space group that seems compatible with our diffraction data; such space group has nevertheless to be confirmed by TEM analysis, outside the scope of this study. A collapse of $a/(2)^{1/2}$ and $b/(2)^{1/2}$ is observed at $T_1 = 325$ °C and $T_1 = 275$ °C for LST and LCST, respectively. It corresponds to the overlapping of the two peaks diffracting at $2\theta \approx 40°$ and referring to (202) and (022) reflections, which is consistent with $a = b$ and illustrates the transition (t_1) from orthorhombic to tetragonal. Then, a second transition is observed at $T_2 = 425$ °C and $T_2 = 375$ °C for LST and LCST, respectively. The three cell parameters become identical. It corresponds to the transition (t_2) from a tetragonal to a cubic perovskite which is consistent with the coalescence of the three peaks diffracting at ~76° in 2θ and referring to (420), (332), and (116) reflections. In reducing atmosphere, the two compositions therefore transform from an orthorhombic to a tetragonal and then to a cubic polymorph when the temperature increases.

Table 1. Structural Parameters of LST and LCST Synthesized at 1400°C/48h in $Ar/H_2(2\%)$ as Determined by the Rietveld Refinement of Powder XRD Data at Room Temperature

$La_{0.33}Sr_{0.67}TiO_{3.04}$ (LST)[a]						
atom	site	*x*	*y*	*z*	U_{iso} (Å^2)	occ.
La	*4j*	0.5	0	0.2522(6)	0.017(2)	0.33
Sr	*4j*	0.5	0	0.2522(6)	0.017(2)	0.67
Ti1	*2c*	0.5	0.5	0	0.011(3)	1
Ti2	*2a*	0	0	0	0.011(3)	1
O1	*8n*	0.270(6)	0.239(7)	0	0.017(2)	1
O2	*4i*	0	0	0.238(7)	0.017(2)	1
$La_{0.23}Ce_{0.10}Sr_{0.67}TiO_{3.04}$ (LCST)[b]						
atom	site	*x*	*y*	*z*	U_{iso} (Å^2)	occ.
La	4j	0.5	0	0.2528(7)	0.026(2)	0.23
Sr	4j	0.5	0	0.2528(7)	0.026(2)	0.67
Ce	4j	0.5	0	0.2528(7)	0.026(2)	0.1
Ti1	2c	0	0.5	0	0.020(3)	1
Ti2	2a	0	0	0	0.020(3)	1
O1	8n	0.275(3)	0.248(7)	0	0.030(3)	1
O2	4i	0	0	0.238(6)	0.030(3)	1

[a] Space group: *Immm* (No. 71), $Z = 4$, $a = 5.5433(3)$ Å, $b = 5.5319(3)$ Å, $c = 7.8165(3)$ Å, $V = 239.69(2)$ Å^3, $R_p = 10.2\%$, $R_{wp} = 14.66\%$, GOF = 0.64, $R_{Bragg} = 2.46\%$. [b] Space Group: *Immm* (No. 71), $Z = 4$, $a = 5.5431(4)$ Å, $b = 5.5284(4)$ Å, $c = 7.8090(5)$ Å, $V = 239.31(3)$ Å^3, $R_p = 7.71\%$, $R_{wp} = 10.49\%$, GOF = 1.58, $R_{Bragg} = 2.39\%$.

Structural Study of LST and LCST versus Temperature in Oxidizing Atmosphere. The same kind of HT-XRD study was carried out in air from RT to 1000 °C. A sudden profile change was

dx.doi.org/10.1021/cm103316b |*Chem. Mater.* 2011, 23, 1539–1550

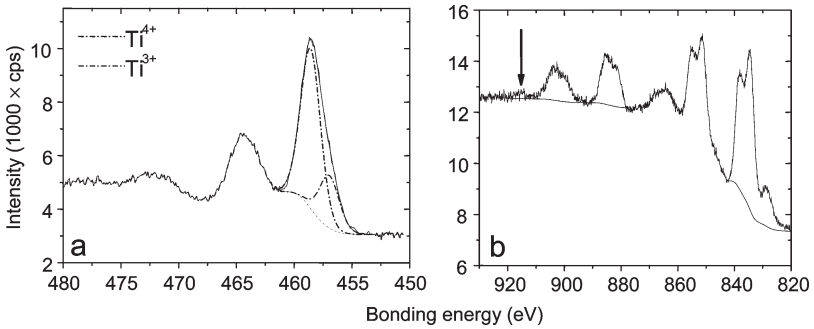

Figure 4. XPS spectra of Ti_{2p} (a) and Ce_{3d} (b) levels of LCST after synthesis at 1400 °C/48 h in $Ar/H_2(2\%)$. The arrow at 915 eV indicates where Ce^{4+} fingerprint should be. Note that the highest energy band in Ti_{2p} spectrum can be deconvoluted into two parts relative to Ti^{3+} and Ti^{4+}.

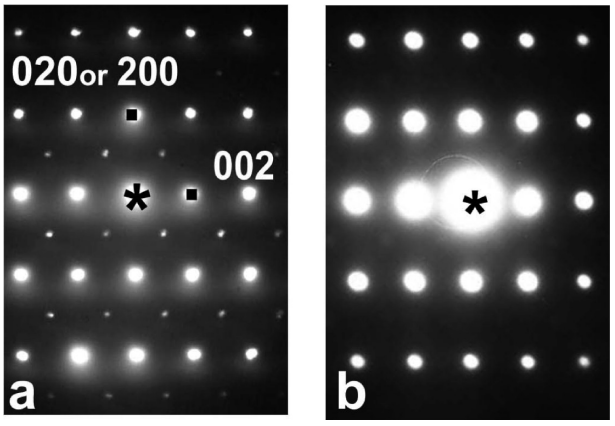

Figure 5. [010] or [100] zone axis pattern of LCST synthesized in $Ar/H_2(2\%)$, indexed in the orthorhombic $(2)^{1/2}a_p \times (2)^{1/2}a_p \times 2a_p$ unit-cell: (a) at room temperature and (b) at 500 °C. The extinction of some spot outlines the structural change from the orthorhombic *Immm* to the cubic $Pm\bar{3}m$ symmetry according to the temperature increase.

observed between 350 and 550 °C for both compositions suggesting a strong decrease in the size of crystalline coherence domains (Figure 8).

The evolution of the normalized lattice volume vs temperature has been obtained from cyclic refinement of HT-XRD data for LST and LCST; for better clarity it is plotted in the last case only in Figure 9 but the same tendency is observed in both cases. The normalized lattice volume used hereafter is defined as the real volume of the lattice divided by the number of formula units per unit cell Z. An accuracy of ±0.01 Å^3 was obtained. During the refinements, the Gaussian and Lorentzian parts of the profile were refined considering the θ-instrumental resolution function of the diffractometer which was deduced from the pattern of an LaB_6 standard (NIST SRM 660a). Apparent crystallite size (which represents the size of coherent domains) was deduced from the β integral breadth of the different reflections based on the evaluation of those Gaussian and Lorentzian parts of the profile.[39] The evolution of the apparent crystallite size vs temperature is plotted for both compounds in the same Figure 9. Between 300 and 500 °C, a strong decrease of the crystallite size is observed whereas the cell volume increases. Then, the crystallite size remains approximately constant until 1000 °C. From about the same temperature range of 500−550 °C, LCST cell volume remains also constant before suffering a small decrease at about 700 °C.

To complete this study and relate those phenomena to oxidation changes, TGA experiments were carried out in air on the reduced samples, allowing us to follow the oxidation process of both materials (Figure 10). LST and LCST undergo a total weight increase of 0.98% and 1.36%, respectively. In good agreement with the HT-XRD study, a deep transformation is observed around 300 °C. It is worth noting that, in contrast to LST, LCST oxidation process is occurring in two steps: the first one corresponds to an approximately 0.9 wt % increase and is located between 350 and 700 °C, in the same range of temperature than for pure LST; the second gain ($\Delta m/m_0 \approx 0.5$ wt %) is observed at higher temperature, between 700 and 1100 °C. Hence, the temperature of each one of the two weight changes are in good agreement with the previously mentioned evolutions of unit-cell volume and crystallite size observed between 300 and 500 °C for both compounds and above 700 °C for LCST (Figure 9).

It is therefore possible to conclude, without any ambiguity, that the first mass gain is due to Ti^{3+} oxidation and the second to Ce^{3+} oxidation. The mass gain of 0.98 wt % for LST corresponds to 24.8% Ti^{3+}, in good agreement with the XPS results. The second step observed in LCST is coherent with the oxidation of the 10% of Ce^{3+}, which would lead to a mass gain of 0.4 wt %.

XRD (Figure 11) and FEG-SEM (Figure 12) were used to analyze the LCST material powder after exposure at 1200 °C for 3 h in air (LCST-ox), simulating the heating treatment usually used to sinter an electrode material. Both techniques reveal the presence of several phases resulting from the decomposition of the initial compound. The main phase is cubic ($Pm\bar{3}m$ space group) and display a cell parameter of a = 3.8966(5) Å (V = 59.147 (5) Å^3). Furthermore, XRD combined with EDS analysis gives evidence of the presence of at least two Ce-rich nanoscaled phases, similarly to the compound prepared in air. Their identification corresponds to CeO_2 and $Ce_{11}O_{20}$ (ICSD No.88758) (Figure 11). Interestingly, re-exposure of the sample to a reducing atmosphere (i.e., 850 °C/48 h in $Ar/H_2(2\%)$) ensured only partial reversibility of this reoxidation and the presence of vacant cavities is observed in place of the previous Ce-rich phases, as illustrated by FEG-SEM images (Figure 13). The detection of residual traces of Ce-enriched phases in the background of the XRD diffractogram (Figure 11) confirms these SEM observations.

Catalytic Activity of LST, LCST, and LCST-ox in CH_4/H_2O Reaction. The catalytic activity of LST and LCST compounds in CH_4/H_2O reaction was measured at 900 °C using a $CH_4/H_2O/N_2$ = 10:1:9 mixture. These conditions have been chosen since being representative of that observed at the inlet of a fuel cell operating on slightly wet methane. They are thermodynamically favorable to the extensive accumulation of carbon. The evolution of the hydrogen concentration at the reactor outlet versus time is

dx.doi.org/10.1021/cm103316b |*Chem. Mater.* 2011, 23, 1539–1550

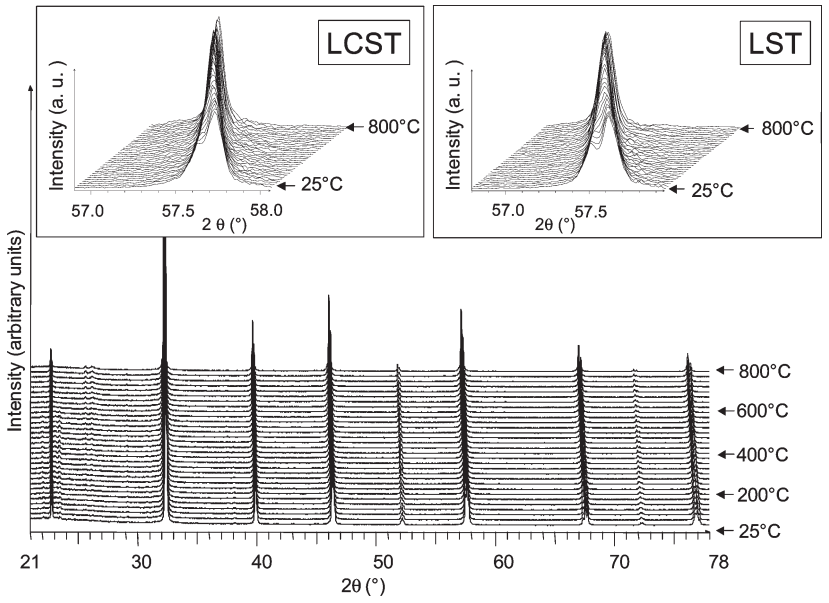

Figure 6. HT-XRD diagrams of LCST in $N_2/H_2(3\%)$. The insets show the evolution of a zoom of the LCST and the LST diagrams from RT to 800 °C.

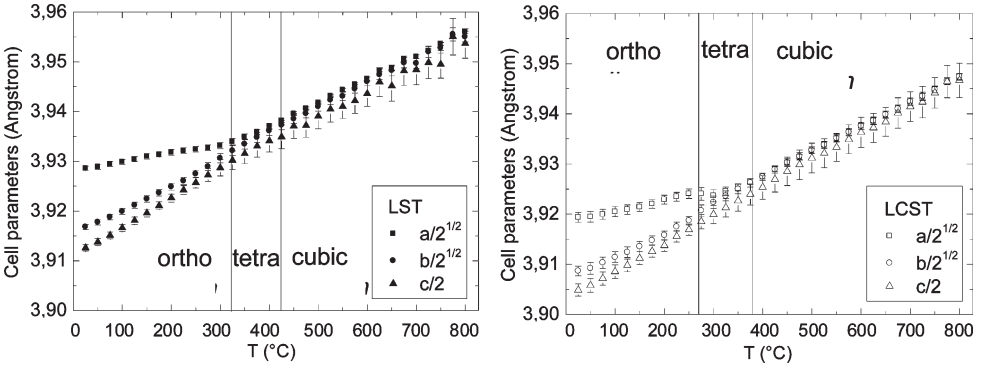

Figure 7. Plot of LST and LCST cell parameters vs temperature in $N_2/H_2(3\%)$, refined in the orthorhombic *Immm* space group, normalized to the equivalent cubic perovskite cell parameters. Error bars correspond to 3σ.

shown in Figure 14 for LST and LCST in reduced state and LSCT in reoxidized state (LCST-ox). CO (not shown in the figure) and H_2 were the main products. It could be derived that LCST-ox was much more active in H_2 production than LST and LCST samples. This cannot be attributed to BET surface area changes, all samples exhibiting approximately the same surface area, equal to ~10 m^2/g (Table 2). Moreover, the catalytic behavior of the LCST-ox sample with time on stream was different from the other two samples. For LST and LCST, the rate of H_2 formation decreased respectively from 2.7 to 1.4 mol h^{-1} g^{-1} and from 1.7 to 0.9 mol h^{-1} g^{-1}, within 4 h reaction. This revealed a slight deactivation of these two samples in the reaction mixture. The deactivation of the reduced LSCT sample seemed to be complete after 4 h reaction, which could not be the case for the LST catalyst. In the case of the LSCT-ox sample, after a sharp drop of the H_2 formation rate in the very first minutes of reaction, a stable steady-state level of H_2 production was rapidly reached. Catalysts deactivation might have various origins such as the decrease of the number or the efficiency of the active sites due to structural changes, poisoning effects, ... The continuous and slight deactivation of reduced LST and LSCT samples, which closely resembles that observed with $Ce_{0.9}Gd_{0.1}O_{2-x}$ (CGO) samples,[40] could be tentatively attributed to the possible further decrease of the BET surface area under reactants or changes in redox properties, as previously demonstrated for CGO activated at 900 °C in N_2.[40] The thermodynamically favored formation of carbon deposits leading to partial poisoning of catalytic sites, as often invoked in CH_4/H_2O reaction, is not excluded. This point was not addressed because of the very low catalytic activity of these samples.

The sharp deactivation of LCST-ox cannot be explained by changes in BET area and/or redox properties, both of these processes being expected to be slow.[40] O_2-TPO experiments performed after catalytic testing over LCST-ox sample revealed the absence of any detectable carbon deposits. The lower limit of CO_2 amount that could be detected by TPO in our experimental conditions was estimated to be less than 1 μmol g^{-1}. Thus the formation of carbon cannot be invoked to explain the sudden drop of activity at initial time. No explanation can be given so far for the transient decrease of LCST-ox activity. However it is worthwhile noticing that (i) even after deactivation, the catalytic activity of LCST-ox is much improved with respect to the other two samples and remarkably stable, (ii) this sample is highly resistant to carbon formation. Both of these properties are of

dx.doi.org/10.1021/cm103316b |*Chem. Mater.* 2011, 23, 1539–1550

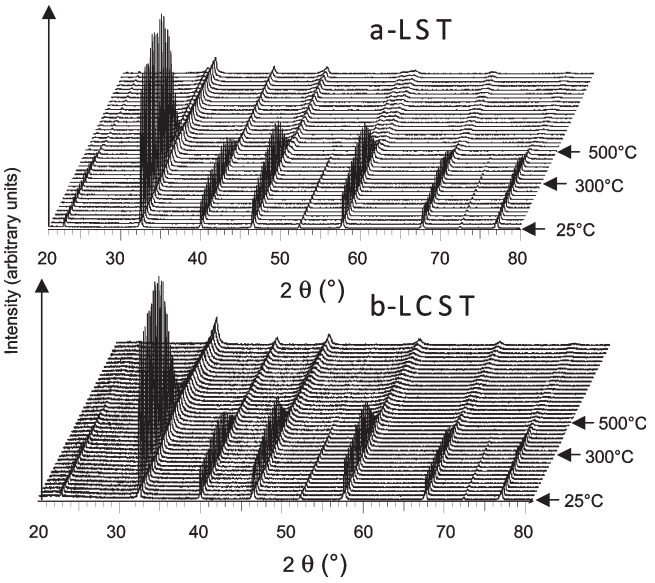

Figure 8. HT-XRD diagrams of *a*-LCST and *b*-LST synthesized at 1400 °C/48 h in Ar/H_2(2%) and exposed to air, recorded from 25 to 1000 °C.

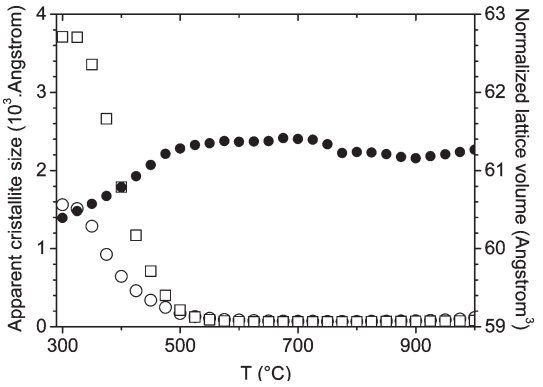

Figure 9. Evolution with temperature in air of the normalized lattice volume of LCST (♦) and the apparent crystallite size of LCST (○) and LST (□), directly after synthesis in Ar/H_2(2%).

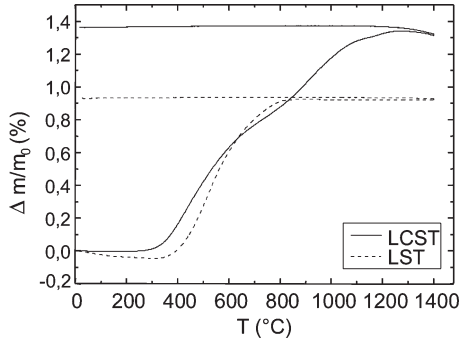

Figure 10. TGA curves in air for LCST (dashed line) and LST (solid line) after synthesis in Ar/H_2(2%).

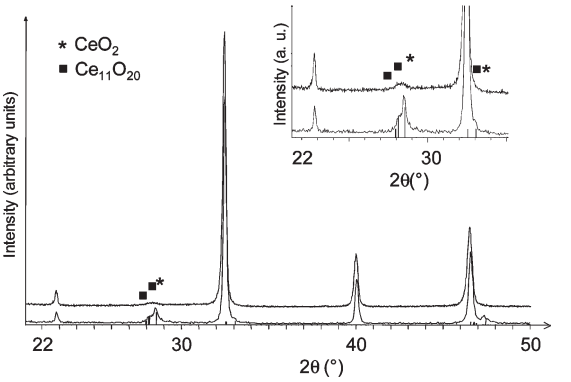

Figure 11. XRD diagrams of LCST after oxidation at 1200 °C in air (bottom) and further reduction at 850 °C/48 h in Ar/H_2(2%) (top). The inset focused on the Ce-enriched phases. Asterisks and squares indicate CeO_2 and $Ce_{11}O_{20}$, respectively.

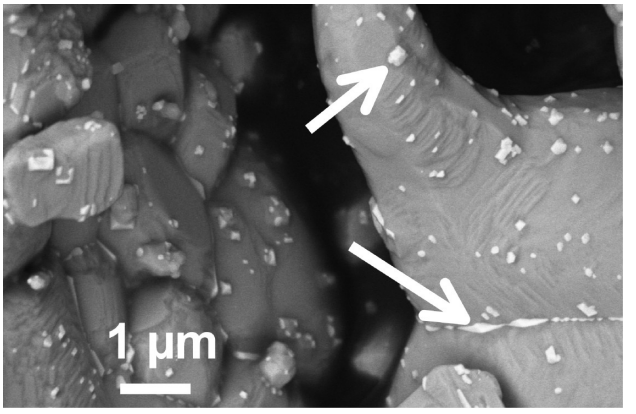

Figure 12. FEG-SEM image in backscattered electron mode of LCST after oxidation at 1200 °C in air. The arrows point at Ce-enriched phases.

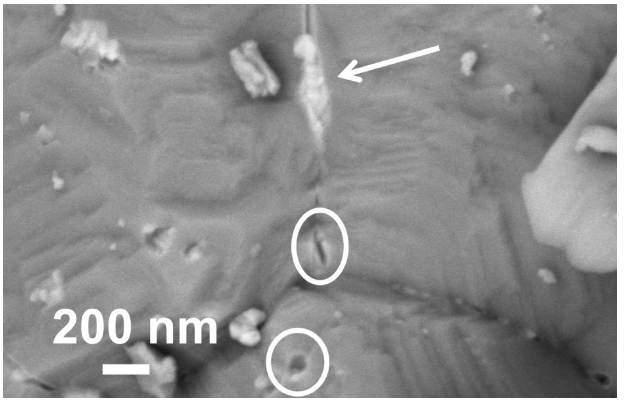

Figure 13. FEG-SEM image in backscattered electron mode of LCST after oxidation at 1200 °C in air and further reduction at 850 °C/48 h in Ar/H_2(2%). The arrow points at a residual Ce-enriched phase, whereas the circles outline the porosity appearing after redissolution of Ce-enriched phases.

interest in view of operating the fuel cell directly with dry or slightly wet methane.

The H_2 formation rates measured after 200 min reaction for LST, LCST and LCST-ox samples are reported in Table 2 and compared with a reference CGO sample treated in N_2 at 900 °C prior to catalyst testing as for the other studied samples. CGO was proposed as a possible anode component due to sufficient catalytic properties in steam reforming when using temperatures above 900 °C.[4,41] The striking feature is that the H_2 formation rate at 900 °C expressed in mol h^{-1} g^{-1} over LCST-ox reached

dx.doi.org/10.1021/cm103316b |*Chem. Mater.* 2011, 23, 1539–1550

Table 2. Specific Surface Area of Catalysts Samples and H_2 Formation Rates

material	specific surface area ($m^2\ g^{-1}$)	pretreatment	flow rate ($L\ h^{-1}$)	H_2 rate[a]	comments
LST	10.5	$N_2/H_2(1\%)$	6.2	1.42	deactivation
LCST	9.7	$N_2/H_2(1\%)$	6.2	0.91	deactivation
LCST-ox	10.6	N_2	6.2	9.35	stabilization after deactivation
CGO[b]	10	N_2	6.5	9.40	deactivation

[a] Formation rates are given in mol $h^{-1}\ g^{-1}$. Measurements were made after 200 min reaction in a $CH_4/H_2O/N_2$ = 10:1:9 gas mixture. [b] Pure gadolinia-doped ceria (CGO) treated in N_2 at 900 °C is used for comparison.

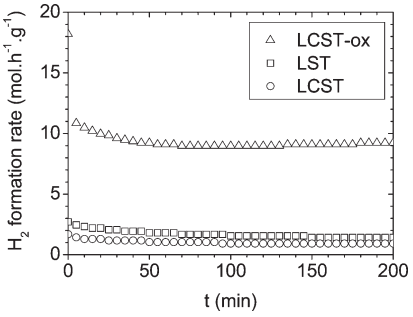

Figure 14. Hydrogen formation rates vs time upon reaction of a 10:1:9 $CH_4/H_2O/N_2$ mixture over LST, LCST and LCST-ox samples. T = 900 °C, 20 mg sample, total dry flow rate = 6.2 L h^{-1}.

that obtained over CGO. Interestingly, only CO formed together with H_2 over the LCST-ox sample while, for CGO, significant CO_2 formation (0.87 mol $h^{-1}\ g^{-1}$) accompanied CO production (2.99 mol $h^{-1}\ g^{-1}$). This indicates that differing catalytic reactions occur on these two samples, which could be due to different catalytic sites. This will be addressed in more details in the Discussion section.

DISCUSSION

Structural Characterization at Room Temperature. The synthesis of LCST compound cannot be achieved in air without the presence of several Ce-rich impurities. Among these, CeO_2 is the only one which is clearly detectable by XRD. The presence of ceria confirms the preference of cerium at the +IV oxidation state under oxidizing atmospheres, but the impossibility to insert, in part or totally, Ce^{4+} in substitution for La^{3+}. This last observation concurs with the literature, where it is reported that, when synthesized in air, titanium perovskite with Ce^{4+} at the A-site has never been observed, in contrast to, for example, cobaltite or Manganite perovskites.[42−44] In perovskite titanates, only the bigger tetravalent cation Th^{4+} (Å)[45] has been encountered at the A site when coupled with monovalent Na^+ in the compound $Na_{2/3}Th_{1/3}TiO_3$.[46] Attempts to synthesize similar material with Ce^{4+} were not conclusive because of the much smaller ionic radius of Ce^{4+} and lower Goldschmidt tolerance factor as compared with that for $Na_{2/3}Th_{1/3}TiO_3$.[46] Furthermore, as confirmed by XPS and XANES, the double perovskite $NaCeTi_2O_6$ involving both Na^+ and exclusively Ce^{3+} also claims in favor of the inexistence of Ce^{4+} cations at the A site of a titanium perovskite.[47] More recently, Ce-doping at the A site of strontium titanate has been successfully obtained but using an A-site deficient stoichiometry in the $Sr_{1-3x/2}Ce_xTiO_3$ series; quite surprisingly for syntheses carried out in air, it has been proved that cerium cations in the series were chiefly 3+.[48,49] In the case of pure (i.e., without cerium) and stoichiometric LST, the presence of $La_2Ti_2O_7$-type impurity in air has already been observed and described in the past. It seems to be related to the accommodation mechanism in air of the oxygen excess associated to donor dopant in strontium titanates.[11,14,50] Such impurities are apparently already present even for low La-content, precipitating in the form of diluted local defects that can grow at a sufficient size to be observed by XRD if the heat treatment is particularly long and high in temperature.

On the other hand, when the synthesis is undertaken in reducing atmosphere such as $Ar/H_2(2\%)$, single phase materials displaying a slightly distorted perovskite structure are obtained for both compositions. Stabilization of the LCST perovskite is easily explained by Ce and Ti at valence +III in such an atmosphere, as attested by XPS measurements. Indeed, Ce^{3+} ionic radius remains close to La^{3+} one (1.34 Å and 1.36 Å with Z = 12, respectively),[45] allowing the achievement of such a substitution, as in the case of $Sr_{1-3x/2}Ce_xTiO_3$ series.[49] In our case, the presence of Ti^{3+} being necessary for charge compensation, reducing atmosphere was required and high temperature increasing entropic term was not sufficient in the Gibbs free energy of formation to allow the synthesis in air of the Ce-doped titanate, contrary to the case of $Sr_{1-3x/2}Ce_xTiO_3$ where Ce^{3+} was demonstrated for a 1400 °C sintering temperature. As shown by XPS and confirmed by TGA, considering the presence of only 25% of Ti^{3+} instead of 33% expected in the case of pure electronic compensation, the developed formula appears to be $La^{+III}_{0.23}Ce^{+III}_{0.1}Sr^{+II}_{0.67}Ti^{+IV}_{0.75}Ti^{+III}_{0.25}O_{3.04}$ and $La^{+III}_{0.33}Sr^{+II}_{0.67}Ti^{+IV}_{0.75}Ti^{+III}_{0.25}O_{3.04}$ for LCST and LST, respectively. It can be noticed that a small excess of overstoichiometric oxygen remains in order to satisfy the electroneutrality of the structure. In contrast to what is generally occurring in most of the perovskites where the B site cation is easily able to change its oxidation state, this interesting observation highlights that charge imbalance led by La^{3+} and Ce^{3+}-substitution is not totally compensated neither by the reduction of Ti from Ti^{4+} to Ti^{3+}[34,51] nor by the creation of cation vacancies.[52,53] Although from a crystallographic point of view, this oxygen excess localization in the compact perovskite structure is not conceivable, no oxygen-overstoichiometric impurity phase has been observed for similar compositions, like $CeTiO_{3+\delta}$[54] and $La_xSr_{1-x}TiO_{3+\delta}$.[14,50] Once again, the explanation is inherent to the presence of local defects of $La_2Ti_2O_7$-type randomly distributed in the structure and not observable by XRD, but which could be outlined for example by TEM.[14]

The full structural characterization required both XRD and SAED technical supports. It is once again worth noticing the importance, in the field of structural studies, to combine different means of analysis such as XRD and SAED, especially when heavy atoms (e.g., Ce and La) coexist with light atoms such as oxygen. Slight TiO_6 distortions coming from weak oxygen atom displacements are less sensitive to X-rays whereas they become obvious using electron diffraction, illustrating the fact that the interaction

between electrons and matter is approximately 10^6 higher than with X-rays. Indeed, in the present study, the use of only X-ray powder diffraction would let us use the approximate *Ibmm* space group, while the combination of TEM and XRD revealed the true space group was *Immm* (#71). As attested by the symmetry similarity between both LST and LCST compounds, the Ti^{3+} concentration seems to be the unique responsible for the presence of a superstructure. A higher ionic radius, as well as a lower oxidation state for the B-site element both generates the same space group and consequently, very similar features (see Table 1).

Thermal Evolution of the Reduced Structure in Reducing or Oxidizing Atmosphere. After synthesis in diluted hydrogen, both LST and LCST remain monophasic during thermal treatment from RT to 1000 °C in the same reducing atmosphere, but undergo two subsequent phase transitions from an orthorhombic to a tetragonal (at $T_1 \approx 300$ °C) and then a cubic symmetry (at $T_2 \approx 400$ °C) when the temperature increases. Such thermally activated phenomenon is quite classical for perovskite structures. It is encountered in many [2 + 4] systems and particularly in Sr or Ca titanates but it generally proceeds in 3 steps following the sequence *Pnma* ↔ *Cmcm* ↔ *I4/mcm* ↔ $Pm\bar{3}m$,[55] what is not the case here with an unusual *Immm* space group at low temperature in both cases but possibly an *I4/mcm* space group at intermediate temperatures, what once again should be confirmed by TEM (see before).

From X-ray thermodiffraction analysis in air of LST and LCST synthesized in reducing atmosphere, we observed a first phenomenon between 400 and 500 °C that seems common to both materials and corresponds, according to TG measurements, to the oxygen uptake via Ti^{3+} reoxidation. As already mentioned, according to the model first described by Bowden et al.[50] and then maintained by other authors,[11,14] the most probable mechanism of accommodation of overstoichiometric oxygen atoms in the structure is related to the formation of more or less extended defects of the $La_2Ti_2O_7$ structure type. If the reoxidation is carried out at much lower temperature (T_{max} = 1000 °C in HT XRD measurements and TGA) than the synthesis or sintering temperature in reducing atmosphere, the precipitation of this lamellar-type impurity that could be described also as planar defects precursor of the $La_2Ti_2O_7$-type phase is occurring in a very diluted form in all the bulk volume of the material; it thus produces strains and a strong decrease of the coherent domains size (at the same time a change in cell volume) for the perovskite, as observed effectively in Figure 9. Bowden et al. have already described such kind of feature but only considering the evolution of the structure in the $Sr_{1-x}La_xTiO_3$ series synthesized at 1350 °C in air, showing exactly the same effect of XRD peaks broadening but as x increase.[50] It can be seen that following another way of preparation (synthesis at high temperature in reducing atmosphere then reoxydation at low temperature in air, for a fixed x composition), we observe the same kind of behavior, that intrinsically reflects the phase diagram of the system.

This crystallite size reduction is a kinetic advantage for an ulterior reduction step (for example during SOFC cell operation) in which the defect can redissolve into the perovskite crystallites with more facility without requiring too high reduction temperature. Such kind of mechanism can also explain why some authors argue on the necessity to prereduced at high temperature La- or Y-doped strontium titanates before processing or using it at lower temperature.[9,11,13,16,19] Even if an intermediate heat treatment in air at $T \approx 1100-1200$ °C for a few hours is required before cell testing (e.g., for cathode elaboration) or if several redox cycles in air at 800−900 °C are applied to the prereduced material to simulate real operation of the cell, the effect on the material structure (and then, in particular, on its electrical properties) will not be dramatic. On the contrary, an air-processed material (synthesis or sintering temperature typically $T > 1300$ °C for titanates) will give rise to so large crystallites size for lamellar impurities that it will never completely disappear in reducing conditions at low temperature due to the low cation diffusion coefficients in oxides; strongly disrupting the structural homogeneity of the sample, the electrical conductivity, measured in reduced atmosphere and at lower operating temperature ($T < 900$ °C) characteristic from the anode ambiance, will remain weak. This phenomenon should be general to donor-doped $SrTiO_3$ materials and not a specificity of LCST for which a second feature seems to appear at higher reoxidation temperature ($T > 700$ °C).

Indeed, to both simulate the sintering treatment of the cathode material and emphasize the phenomenon that seems to occur during the oxidation above 700 °C, LCST powder was exposed to a calcination in air at 1200 °C for 3 h. The powder XRD pattern reveals the presence of at least two phases: the main cubic phase, a substoichiometric perovskite similar to $La_{0.23}\square_{0.1}Sr_{0.67}TiO_3$, which results from the exsolution of Ce as CeO_2. However, some nonindexed peaks remain at around $2\theta = 28°$. According to the initial stoichiometry of the compound, a possible indexation is $Ce^{+III}{}_4Ce^{+IV}{}_7O_{20}$.[56] But, as demonstrated by TGA, no Ce^{3+} remains after air exposure at 1200 °C/3 h. One explanation of the presence of this phase leads to consider the formation of the similar phase $La^{+III}{}_4Ce^{+IV}{}_7O_{20}$. This hypothesis involves also the exsolution of a small amount of La^{3+}, which calculated proportion corresponds to 0.01 La^{3+} to form $La_{0.22}Sr_{0.67}TiO_3$, the x = 0.22-compound of the neighbored family $La_xSr_{1-1.5x}TiO_3$. To sum up, the oxidation of LCST could correspond to the following reaction:

$$La_{0.23}Ce_{0.1}Sr_{0.67}TiO_{3.04} + 0.0875O_2 \rightarrow La_{0.22}Sr_{0.67}TiO_3 + 0.0825CeO_2 + 0.0025La_4Ce_7O_{20} \quad (1)$$

XRD pattern refinement of the main phase supports this hypothesis. Indeed, the main cubic phase displays a cell parameter of a = 3.8966(5) Å in the $Pm\bar{3}m$ space group, identical to the theoretical value of 3.8966 Å calculated from the Vegard's law between $SrTiO_3$ and $La_{2/3}TiO_3$ ($y = 3.905 - 0.03825x$), according to R. Moos et al.[52]

FEG-BSE images recorded on the sample exposed to air at 1200 °C for 3 h are in good agreement with the XRD data. The BSE images outline the chemical contrast existing between the main phase and the segregated electron-enriched phases located at the grain boundaries. Furthermore, EDS analyses confirm the enrichment in Ce of the segregated phases, since the peaks relative to cerium are more important when the analysis is focused on the exsoluted phases than on the bulk material. Such a phenomenon can be named "exsolution" or precipitation of cerium oxides nanoparticles at the surface of the titanate micrometer scale grains, that could be particularly interesting for catalytic properties (oxidation or reforming of hydrocarbon molecules),[21,57−60] but also for the electrocatalytic oxidation of hydrogen[3] due to the high chemical reactivity conferred to the material (Figure 12). Such a phenomenon, once again well-known because already used to synthesize metallic (e.g., Ni) nanoparticles-based catalysts,[61−63] has been recently applied to

the development of new anode materials.[64−67] On the contrary of the latest examples, the catalytically interesting nanoceria phase is obtained in our case by reoxidation in air (simulating the necessary sintering of the air electrode) of the previously pure titanate obtained by synthesis at high temperature in reducing conditions, and not by reduction of a pure air-synthesized oxide.

To complete the study and simulate a real SOFC anode cycle, the latter material was exposed to $Ar/H_2(2\%)$ at 850 °C for 48 h. FEG-BSE images show the partial reversibility of the exsolution process, allowing to affirm that some ceria nanoparticles will remain in real anodic conditions (less reducing than dry $Ar/H_2(2\%)$ at OCV, and more oxidant under anodic polarization). The detection of residual traces of Ce-enriched phases in the background of the XRD pattern confirms the microscopy observations, so that we have to consider a phase of intermediate Ce content, comprised between the reduced form of *Immm*-LCST and the fully oxidized form of $Pm\bar{3}m$-LCST. The refinement in the $Pm\bar{3}m$ space group led to a volume $V_{Pm\bar{3}m}$, which was superior to the value of the fully oxidized LCST ($V_{Pm\bar{3}m}$ = 59.428(4) Å^3 instead of 59.147(5) Å^3), attesting to the solely partial reinsertion of the Ce cation into the structure, and so the presence along the grain boundaries of residual Ce-enriched phases (especially CeO_2) that can improve both the catalytic and electrocatalytic properties of the material.

Finally, one could argue that the synthesis in reducing conditions of LCST is an additional difficulty in comparison to other materials, but it is worth noting that due to the necessity to reduce any donor-doped titanate at high temperature (during synthesis or sintering of the anodic layer) to obtain a sufficiently high electronic conductivity and use it as an anode, this is not in reality the case.

Relationship between LCST Structure and Catalytic Behavior in CH_4/H_2O Reaction. The catalytic conversion of CH_4/H_2O mixtures at 900 °C can proceed through many equilibrated reactions as listed below by considering the forward reactions thermodynamically favored from the left to the right:

$$CH_4 \leftrightarrows C + 2H_2 \text{ (methane cracking)} \quad (2)$$

$$CH_4 + H_2O \leftrightarrows CO + 3H_2 \text{ (steam reforming)} \quad (3)$$

$$CH_4 + 2H_2O \leftrightarrows CO_2 + 4H_2 \text{ (reverse methanation)} \quad (4)$$

$$CO_2 + H_2 \leftrightarrows CO + H_2O \text{ (reverse water gas shift)} \quad (5)$$

$$CH_4 + CO_2 \leftrightarrows 2CO + 2H_2 \text{ (dry methane reforming)} \quad (6)$$

$$C + H_2O \leftrightarrows CO + H_2 \quad (7)$$

$$C + 2H_2O \leftrightarrows CO_2 + 2H_2 \quad (8)$$

$$C + CO_2 \leftrightarrows 2CO \text{ (reverse Boudouard reaction)} \quad (9)$$

On the basis of thermodynamics calculations, it can be stated that, at the equilibrium at 900 °C, starting from a gas composition of 50% CH_4, 5% H_2O, N_2 balance, CH_4 and H_2O are both almost totally converted, producing H_2, CO, and C. This suggests that, in these conditions, thermodynamics would be essentially governed by steam reforming (consuming both methane and steam) and methane cracking (consuming methane but producing large amounts of solid carbon). The absence of such carbon deposits upon CH_4/H_2O reaction over LSCT-ox at 900 °C clearly indicates that reactions proceed under kinetic control over this catalyst.

It is also clear from our experimental data that, whereas the incorporation of Ce into the LST structure (LCST) has a negative impact on the catalytic production of H_2, the exsolution of nanosized Ce-rich particles upon oxidative treatment of LCST (LCST-ox) enhances the catalytic activity by 1 order of magnitude. It is worthwhile noticing that the catalytic formation of H_2 over LCST-ox is similar to that of pure CGO, although catalytic sites are likely different because of different structures and composition. In CH_4/H_2O reaction, the rate limiting step involves the activation of the highly stable methane molecule irrespective of the metallic or oxidic nature of the catalyst. This is consistent with the first order rate of the H_2 production with respect to methane partial pressure.[70,71] There has been a general agreement in the literature to conclude that the mechanism of CH_4/H_2O reaction over ceria based materials proceeds according to the following two steps:

(i) A step of ceria reduction by reaction with methane, thus producing oxygen vacancies and Ce^{3+} ions.
(ii) A step involving H_2O and leading to the reoxidation of Ce^{3+} into Ce^{4+} ions with refilling of oxygen vacancies by oxygen ions.

In this view, the production of carbon species acting as an intermediate in the global reaction such as on Ni catalysts is not considered, thus explaining the high resistance of these oxide materials to carbon formation even in severe coking conditions. The mechanism by which methane activation proceeds over oxide materials remains unclear however. Accordingly, reaction 3 (steam reforming) is basically assumed to proceed over ceria based materials. However, some CO_2 formation can be also observed.[40] This suggests that catalytic sites over ceria based materials may also catalyze other reactions than only steam reforming. Since reactions involving C can be all excluded (see previous arguments) and reverse water gas shift reaction is favored at 900 °C, CO_2 is mainly expected to form through reaction 4 (reverse methanation), which would involve the production of CO_2 instead of CO in the first step of the above mechanism involving methane as a reactant. This is not unlikely owing to the known property of ceria to easily fully oxidize hydrocarbons.[21,68] In this respect the catalytic behavior of LSCT-ox and therefore of the catalytic sites present at the surface of this composite material are likely different from that present at the CGO surface, being less oxidizing than on ceria based systems. Considering the composite nature of this material with at least two different phases, the main cubic phase, a substoichiometric perovskite similar to $La_{0.23}\square_{0.1}Sr_{0.67}TiO_3$, and a Ce-enriched phase, it could be proposed that

(i) The Ce-enriched phase is mainly responsible for the observed catalytic activity improvement with respect to LST phase.
(ii) The Ce-enriched phase is different in nature from pure ceria since no CO_2 could form.

Considering electron micrographs, it can be stated that most of the surface area of the composite LSCT-ox sample is because of the main fraction of the material (90%) having the perovskite structure. Consequently most exposed surface sites would negligibly contribute to the catalytic activity in agreement with literature data reporting the poor catalytic properties of the $La_xSr_{1-3x/2}TiO_3$ family.[69] On the contrary, the minor Ce-enriched phase, contributing to much less than 10 m^2/g, would be as active

as 10 m^2/g of pure CGO. This could be tentatively attributed to a size effect on catalytic properties, this active phase being dispersed as nanoscaled particles segregated at the grain boundaries.[57−60] LCST-ox catalytic behavior in CH_4/H_2O reaction could be compared to that of SYT-CeO_2.[21,22]

This study finally highlights the major effect of the cerium environment on the catalytic properties in CH_4/H_2O reaction for producing H_2. An excessive stabilization of Ce^{3+} ions in the perovskite structure such as in LCST structure after reducing treatment where Ce is stabilized in 12-fold coordination sites, does not provide any significant catalytic activity in H_2 production from CH_4/H_2O mixtures. On the contrary, the Ce-enriched phase would exhibit improved redox properties, likely through Ce^{4+}/Ce^{3+} couple, in a way similar or even easier than in ceria-based materials.

Therefore, developing a phase catalytically active in CH_4 activation or H_2 production from CH_4 on the top of a good electronic conductor, such as in the LSCT-ox sample, could be a promising route in view of developing anode materials for fuel directly operating on methane.

CONCLUSIONS

Under reducing condition, the insertion of Ce^{3+} at the La site of the $La_xSr_{1-x}TiO_{3+\delta}$ ($x = 0.33$) (LST) titanate was proved to be possible. A $La_{0.23}Ce_{0.1}Sr_{0.67}TiO_{3+\delta}$ (LCST) pure phase was prepared. As LST, its symmetry at room temperature is orthorhombic of space group *Immm*. In $N_2/H_2(3\%)$, it subsequently transforms to a tetragonal then a cubic polymorph, at 275 and 375 °C, respectively.

The oxidation in air of LCST leads to two features:

(i) As in LST, Ti^{3+} cations reoxidize to Ti^{4+} producing a strong decrease in the crystallite size of the perovskite probably because of the precipitation of a lamellar-type impurity (extended defects precursor of the $La_2Ti_2O_7$-type impurity) that accommodates the oxygen excess.

(ii) A decomposition into a multiphased system containing Ce-enriched phases segregated at the grain boundaries of the conducting titanate. This ceria exsolution is not completely reversible in SOFC anodic conditions.

This exsolution phenomenon allows the enhancement of the catalytic activity in methane steam reforming by 1 order of magnitude with respect to the starting material. Interestingly this material reveals a high resistance to carbon formation, which makes this material a good candidate for a SOFC anode working directly in methane. The measurement of the electrical properties of this anode material is currently in progress, as well as the study of the electrochemical properties in H_2/H_2O.

AUTHOR INFORMATION

Corresponding Author

*E-mail: gilgau@uis.edu.co. Phone: (+57) 634 4000, ext. 2528. Fax: (+57) 634 4684.

Present Addresses

⊥Universidad Industrial de Santander, Escuela de Ingeniería Química, Bucaramanga, Colombia.

ACKNOWLEDGMENT

The authors are grateful to M. Frère for XPS experiments and A. Montani for FEG-SEM analysis. C.P.-M. is grateful to ADEME and CEA for the PhD funding. The TEM and XRD facilities in Lille (France) are supported by the Conseil Regional du Nord-Pas de Calais, and the European Regional Development Fund (FEDER).

REFERENCES

(1) Steele, B. C. H. *Solid State Ionics* **1996**, *86−88*, 1223.
(2) Pudmich, G.; Boukamp, B. A.; González-Cuenca, M.; Jungen, W.; Zipprich, W.; Tietz, F. *Solid State Ionics* **2000**, *135*, 433.
(3) Atkinson, A.; Barnett, S.; Gorte, R. J.; Irvine, J. T. S.; McEvoy, A. J.; Mogensen, M.; Singhal, S. C.; Vohs, J. *Nat. Mater.* **2004**, *3*, 17.
(4) McIntosh, R. S.; Gorte, R. J. *Chem. Rev.* **2004**, *104*, 4845 and references therein.
(5) Vernoux, P.; Guindet, J.; Kleitz, M. *J. Electrochem. Soc.* **1998**, *145*, 3487.
(6) Mogensen, M. *Proceedings of the 26th Risø International Symposium on Materials Science*; Linderoth, S. et al.., Eds.; Risø National Laboratory: Roskilde (DK), 2005; p 51.
(7) Marina, O. A.; Canfield, N. L.; Stevenson, J. W. *Solid State Ionics* **2002**, *149*, 21.
(8) Hui, S.; Petric, A. *J. Electrochem. Soc.* **2002**, *149*, J1.
(9) Canales-Vásquez, J.; Tao, S. W.; Irvine, J. T. S. *Solid State Ionics* **2003**, *159*, 159.
(10) Mukundan, R.; Brosha, E. L.; Garzon, F. H. *Electrochem. Solid-State Lett.* **2004**, *7*, A5.
(11) Hashimoto, S.; Kindermann, L.; Poulsen, F. W.; Mogensen, M. *J. Alloys Compd.* **2005**, *397*, 245. Hashimoto, S.; Kindermann, L.; Larsen, P. H.; Poulsen, F. W.; Mogensen, M. *J. Electroceram.* **2006**, *16*, 103.
(12) Pillai, M. R.; Kim, I.; Bierschenk, D. M.; Barnett, S. A. *J. Power Sources* **2008**, *185*, 1086.
(13) Fu, Q. X.; Tietz, F. *Fuel Cells* **2008**, *8* (5), 283.
(14) Canales-Vásquez, J.; Smith, M. J.; Irvine, J. T. S.; Zhou, W. *Adv. Funct. Mater.* **2005**, *15*, 1000.
(15) Ruiz-Morales, J. C.; Canales-Vásquez, J.; Savaniu, C.; Marrero-López, D.; Zhou, W.; Irvine, J. T. S. *Nature* **2006**, *439*, 568.
(16) Fu, Q.; Tietz, F.; Sebold, D.; Tao, S.; Irvine, J. T. S. *J. Power Sources* **2007**, *171*, 663.
(17) Lee, S.; Kim, G.; Vohs, J. M.; Gorte, R. J. *J. Electrochem. Soc.* **2008**, *155*, B1179.
(18) Sun, X.; Wang, S.; Wang, Z.; Qian, J.; Wen, T.; Huang, F. *J. Power Sources* **2009**, *187*, 85.
(19) Ma, Q.; Tietz, F.; Leonide, A.; Ivers-Tiffée, E. *J. Power Sources* **2011**, doi:10.1016/j.jpowsour.2010.07.094.
(20) Steele, B. C. H.; Middleton, P. H.; Rudkin, R. A. *Solid State Ionics* **1990**, *40−41*, 388.
(21) Trovarelli, A. *Catal. Rev.-Sci. Eng.* **1996**, *38*, 439.
(22) Koutcheiko, S.; Yoo, Y.; Petric, A.; Davidsoon, I. *Ceram. Int.* **2006**, *32*, 67.
(23) Gorte, R. J.; Vohs, J. M.; McIntosh, S. *Solid State Ionics* **2004**, *175*, 1.
(24) Gross, M. D.; Vohs, J. M.; Gorte, R. J. *Electrochem. Solid-State Lett.* **2007**, *10*, B65.
(25) Kim, G.; Corre, G.; Irvine, J. T. S.; Vohs, J. M.; Gorte, R. J. *Electrochem. Solid-State Lett.* **2008**, *11*, B16.
(26) Kim, G.; Lee, S.; Shin, J. Y.; Corre, G.; Irvine, J. T. S.; Vohs, J. M.; Gorte, R. J. *Electrochem. Solid-State Lett.* **2009**, *12*, B48.
(27) Marina, O. A.; Pederson, L. R. *Proceedings of the 5th European SOFC Forum*;Huijsmans, J., Ed.; European Fuel Cell Forum: Lucerne, CH, 2002, p 481.
(28) Marina, O. A.; Stevenson, J. W. *Proceedings of Solid State Ionic Devices III*; Wachsman, E. D. et al. , Eds.; PV 2002−26; The Electrochemical Society: Pennington, NJ, 2002; p 91.
(29) Koutcheiko, S.; Yoo, Y.; Petric, A.; Davidsoon, I. *Proceedings of the 5th European SOFC Forum*; Huijsmans, J. (Ed.); European Fuel Cell Forum: Lucerne, CH, 2002; p 655.
(30) Mao, C.; Dong, X.; Zeng, T. *Mater. Lett.* **2007**, *61*, 1633.
(31) Rodriguez-Carjaval, J. *Phys. B* **1993**, *192*, 55. Rodríguez-Carvajal, J. *Comm. Powder Diffr. (IUCr) Newsl.* **2001**, *26*, 12.

(32) Glazer, A. M. *Acta Crystallogr. B* **1972**, *28*, 3384.
(33) Barth, T. *Norsk Geol. Tidsskrift* **1925**, *8*, 201.
(34) Sunstrom, J. E., IV; Kauzlarich, S. M.; Klavins, P. *Chem. Mater.* **1992**, *4*, 346.
(35) Sunstrom, J. E., IV; Kauzlarich, S. M.; Antonio, M. R. *Chem. Mater.* **1993**, *5*, 182.
(36) Mullins, D. R.; Overbury, S. H.; Huntley, D. R. *Surf. Sci.* **1998**, *409*, 307.
(37) Nédélec, J. M.; Gengembre, L.; Turell, S.; Bouazaoui, M.; Grimblot, J. *Appl. Surf. Sci.* **1999**, *142*, 243.
(38) Mayer, J. T.; Diebald, U.; Madley, T. E.; Garfunkel, E. *J. Electron Spectrosc. Relat. Phenom.* **1995**, *73*, 1.
(39) De Keijser, T. H.; Langford, J. I.; Mittemeijer, E. J.; Vogels, A. B. P. *J. Appl. Crystallogr.* **1982**, *15*, 308.
(40) Mosqueda, B.; Toyir, J.; Kaddouri, A.; Gélin, P. *Appl. Catal. B: Environ.* **2009**, *88*, 361.
(41) Ramirez-Cabrera, E.; Atkinson, A.; Chadwick, D. *Appl. Catal. B: Environ.* **2002**, *36*, 193.
(42) Fuchs, D.; Schweiss, P.; Adelmann, P.; Schwarz, T.; Schneider, R. *Phys. Rev. B* **2005**, *72*, 014466.
(43) Zeng, Z.; Greenblatt, M.; Croft, M. *Phys. Rev. B* **2001**, *63*, 224410.
(44) Kang, J.-S.; Kim, Y. J.; Lee, B. W.; Olson, C. G.; Min, B. I. *J. Phys.: Condens. Matter* **2001**, *13*, 3779.
(45) Shannon, R. D.; Prewitt, C. T. *Acta Cryst. B* **1969**, *25*, 925.
(46) Zhu, W. J.; Hor, P. H. *J. Solid State Chem.* **1995**, *120*, 208.
(47) Wright, C. S.; Walton, R. I.; Thompsett, D.; Fisher, J. *Inorg. Chem.* **2004**, *43*, 2189.
(48) Subodh, G.; James, J.; Sebastian, M. T.; Paniago, R.; Dias, A.; Moreira, R. L. *Chem. Mater.* **2007**, *19*, 4077.
(49) Ubic, R.; Subodh, G.; Gout, D.; Sebastian, M. T.; Proffen, T. *Chem. Mater.* **2010**, *22* (6), 2174.
(50) Bowden, M. E.; Jefferson, D. A.; M. Brown, I. W. *J. Solid State Chem.* **1995**, *117*, 88.
(51) Eylem, C.; Sághi-Szabó, G.; Chen, B. H.; Eichhorn, B.; Peng, J. L.; Greene, R.; Salamanca-Riba, L.; Nahm, S. *Chem. Mater.* **1992**, *4*, 1038.
(52) Moos, R.; Bischoff, T.; Menesklou, W.; Härdtl, K. H. *J. Mater. Sci.* **1997**, *32*, 4247.
(53) Markovec, D.; Samardzija, Z.; Delalut, U.; Kolar, D. *J. Am. Ceram. Soc.* **1995**, *78* (8), 2193.
(54) Katsufuji, T.; Tokura, Y. *Phys. Rev. B* **2000**, *62*, 10797.
(55) Mitchell, R.H., *Perovskites: Modern and Ancient*; Almaz Press Inc.: Thunder Bay, ON, CA, 2002; pp 39−41 and references therein.
(56) Kümmerle, E. A.; Heger, G. *J. Solid State Chem.* **1999**, *147*, 485.
(57) Garcia, T.; Solsona, B.; Taylor, S. H. *Catal. Lett.* **2005**, *105*, 183.
(58) Laosiripojanaa, N.; Assabumrungrat, S. *Chem. Eng. Sci.* **2006**, *61*, 2540.
(59) Ntainjua Ndifor, E.; Garcia, T.; Solsona, B.; Taylor, S. H. *Appl. Catal. B: Environ.* **2007**, *76*, 248.
(60) Hosseinpour, N.; Ali Khodadadi, A.; Mortazavi, Y.; Bazyari, A. *Appl. Catal. A: Gen.* **2009**, *353*, 271.
(61) Shiozaki, R.; Andersen, A. G.; Hayakawa, T.; Hamakawa, S.; Suzuki, K.; Shimizu, M.; Takehira, K. *Stud. Surf. Sci. Catal.* **1997**, *110*, 701.
(62) Batiot-Dupeyrat, C.; Sierra Gallego, G. A.; Mondragón, F.; Barrault, J.; Tatibouët, J. M. *Catal. Today* **2005**, *107*−*108*, 474.
(63) Mawdsley, J. R.; Krause, T. R. *Appl. Catal. A: Gen.* **2008**, *334*, 311.
(64) Madsen, B. D.; Kobsiriphat, W.; Wang, Y.; Marks, L. D.; Barnett, S. A. *ECS Trans.* **2007**, *7*, 1339.
(65) Kobsiriphat, W.; Madsen, B. D.; Wang, Y.; Marks, L. D.; Barnett, S. A. *Solid State Ionics* **2009**, *180*, 257.
(66) Jardiel, T.; Caldes, M. T.; Moser, F.; Hamon, J.; Gauthier, G.; Joubert, O. *Solid State Ionics* **2010**, *181*, 894.
(67) Kobsiriphat, W.; Madsen, B. D.; Wang, Y.; Shah, M.; Marks, L. D.; Barnett, S. A. *J. Electrochem. Soc.* **2010**, *157*, B279.
(68) Trovarelli, A. *Catalysis by Ceria and Related Materials*, Catalytic Science Series, Vol. 2; Hutchkings, G. J., Ed.; Imperial College Press: London, U.K., 2002; pp 15−50.
(69) Slater, P. R.; Fagg, D. P.; Irvine, J. T. S. *J. Mater. Chem.* **1997**, *7*, 2495.
(70) Wei, J.; Iglesia, E. *J. Catal.* **2004**, *224*, 370.
(71) Ramirez-Cabrera, E.; Atkinson, A.; Chadwick, D. *Appl. Catal. B: Environ.* **2004**, *47*, 127.